Appl. Phys. A (2016) 122:550
DOI 10.1007/s00339-016-0082-z

Applied Physics A
Materials Science & Processing

Influence of Ni substitution at B-site for Fe^{3+} ions on morphological, optical, and magnetic properties of $HoFeO_3$ ceramics

Zubida Habib[1] · Kowsar Majid[1] · Mohd. Ikram[2] · Khalid Sultan[2] · Sajad Ahmad Mir[2] · K. Asokan[3]

Received: 12 January 2016 / Accepted: 18 April 2016 / Published online: 2 May 2016

Abstract Present study reports the effect of Ni substitution at B-site in $HoFeO_3$ on the morphological, optical and magnetic properties. These compounds were prepared by solid-state reaction method. Scanning electron microscope reveals an increase in average grain sizes with Ni concentration. Absorption and emission spectra show redshift in band gap with increase in Ni ion concentrations. The Tauc plots show direct allowed transitions. Temperature-dependent magnetization studies on these compounds revealed the transition from ferromagnetism to paramagnetism. There is separation between temperature at which zero-field-cooled and field-cooled occurs at varied temperature with Ni substitution. The separation effect is related to the impact of the paramagnetic Ho^{3+} ions, whose magnitude becomes more prominent at higher temperature. The value of squareness ratio in these materials is below 0.5 indicating presence of multidomain structures.

1 Introduction

There has been considerable interest in perovskite-type compounds both for scientific and technological reasons in recent years. The rare earth orthoferrites, $RFeO_3$, have well-defined magnetic properties and are a well-studied family of magnetic materials [1]. These materials exhibit a variety of physical properties, such as dielectric, magnetic, optical, and transport properties, owing to strong electron correlation and the discovery of the metal–insulator transition (MIT), and charge ordering [2–6]. $RFeO_3$ crystallizes in an orthorhombically distorted perovskite structure with space group *Pbnm* and exhibit weak ferromagnetism above room temperature [9]. The magnetic properties of these oxides have been extensively studied by Neel and other authors [10–12]. These are essentially antiferromagnetic, but tend to exhibit a weak parasitic ferromagnetism, which is an intrinsic property of the iron sublattice of the perovskite structure and disappears at a temperature of about 700 K (Neel temperature). These properties are due to the following contributions: (i) preferential ordering of impurities or defects into alternate (111) planes of the antiferromagnetic iron octahedral sublattice (ii) interstitial Fe ions in inhomogeneity-induced regions of high iron concentration (iii) Fe^{3+} spins canted in a common direction mainly by anisotropic super exchange and (iv) canting of the antiferromagnetic rare earth sublattice due to the interactions between the two 12-coordinated and octahedral sublattices [6–12]. Doping of Ni in $LaFeO_3$ and $PrFeO_3$ up to the critical concentration leads to properties like the insulator–metal transition and ferromagnetic to paramagnetic transition and stabilizes the magnetic structure by reducing the asymmetry in hysteresis [13, 14]. The magnetic interaction between the Fe^{3+} and Ni^{3+} states may lead to interplay with the intrinsic magnetic behavior of the rare earth sublattices at low temperature [15, 16].

The crystalline symmetry of $HoFeO_3$ is described by the orthorhombic space group *Pbnm* with unit cell dimensions $a = 5.284$, $b = 5.589$ and $c = 7.608$ Å and contains four distorted perovskite units [17]. Based on neutron

✉ Mohd. Ikram
ikram@nitsri.net

[1] Department of Chemistry, National Institute of Technology, Hazratbal, Srinagar 190006, India

[2] Department of Physics, National Institute of Technology, Hazratbal, Srinagar 190006, India

[3] Inter University Accelerator Centre, Aruna Asaf Ali Marg, New Delhi 110067, India

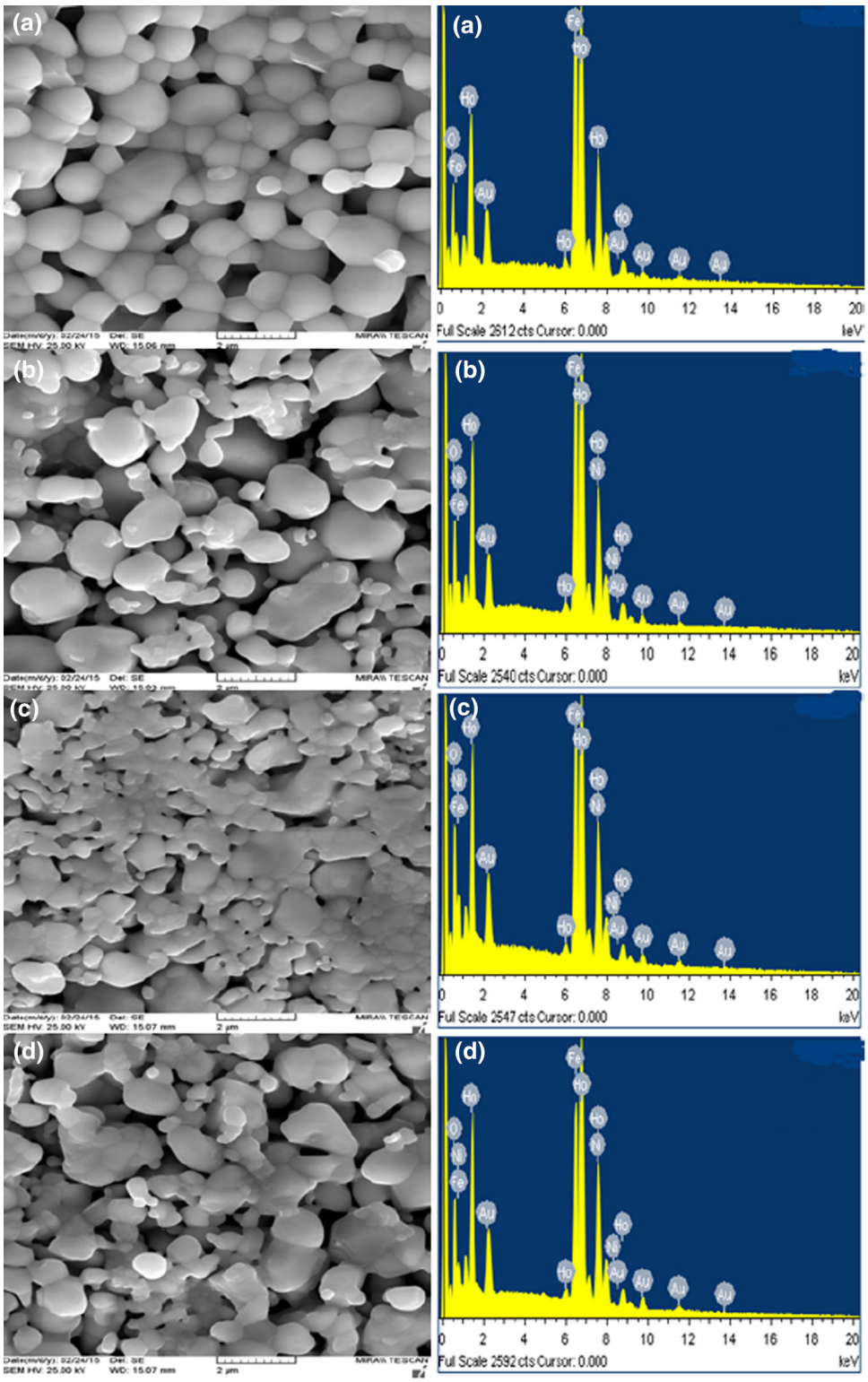

Fig. 1 SEM micrograph and EDAX spectra o fHoFe$_{1-x}$Ni$_x$O$_3$ ($x = 0.0, 0.1, 0.3, 0.5$)

diffraction studies, it has been reported that the net magnetic moment of $HoFeO_3$ becomes parallel to the magnetic moment of Fe^{3+} below at about 60 K and its magnitude increases rapidly with decrease of temperature down to the liquid He temperature [18]. Distorted antiferromagnetic ordering of Ho^{3+} ions at 6.5 K and a canted antiferromagnetic ordering of Fe^{3+} ions at 700 K was observed later [19]. The spin reorientation transition at around 50 K

Table 1 Theoretical and experimental weight percentage of Ho, Fe, and Ni as obtained by EDAX

Compound	Element	Experimental (weight %)	Theoretical (weight %)
$HoFeO_3$	O	19.90	17.85
	Fe	19.17	20.81
	Ho	60.93	61.35
$HoFe_{0.9}Ni_{0.1}O_3$	O	20.19	17.83
	Ni	1.87	2.15
	Fe	18.02	18.71
	Ho	59.92	61.30
$HoFe_{0.7}Ni_{0.3}O_3$	O	19.82	17.80
	Ni	5.78	6.45
	Fe	15.17	14.53
	Ho	59.23	61.21
$HoFe_{0.5}Ni_{0.5}O_3$	O	18.69	17.78
	Ni	9.27	10.73
	Fe	11.53	10.36
	Ho	60.51	61.12

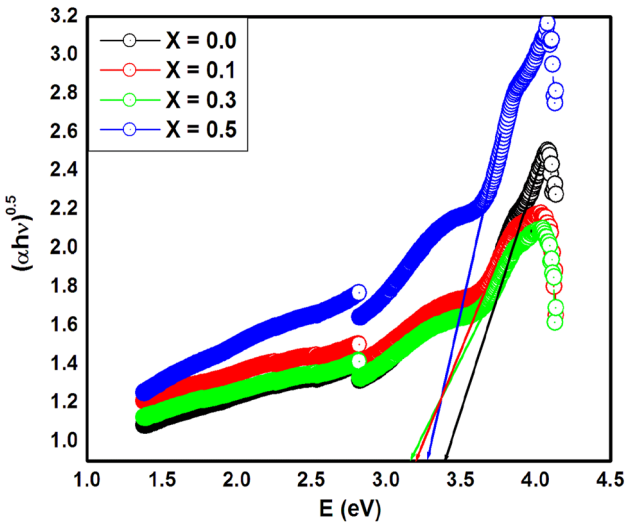

Fig. 2 Tauc plot of $HoFe_{1-x}Ni_xO_3$ ($x = 0.0, 0.1, 0.3, 0.5$)

Table 2 Band gap energy of $HoFe_{1-x}Ni_xO_3$ ($x = 0.0, 0.1, 0.3, 0.5$)

Composition (x)	Band gap energy (eV)
0.0	3.39
0.1	3.20
0.3	3.17
0.5	3.28

was also investigated [20]. Neel temperature (T_N) of the $HoFeO_3$ is known to be ~640 K [21, 22].

Present study focuses on the effect of Ni doping at Fe site on $HoFeO_3$ with reference to its morphology, optical and magnetic properties.

2 Experimental details

Solid-state reaction technique was used to prepare the bulk samples of $HoFe_{1-x}Ni_xO_3$ ($x = 0.0, 0.1, 0.3, 0.5$). The precursors Ho_2O_3, Fe_2O_3, and NiO (each of purity 99.9 %) were weighed on a digital analytical balance according to the stoichiometric ratio after the appropriate calculations. The weighed quantities of these desired powder samples were thoroughly and repeatedly ground in presence of acetone (to improve homogeneity) using agate mortar and pestle. The resultant powders were then pre-calcinated at 1000 °C for 12 h and again ground and calcinated at 1200 °C for 12 h. Finally, the samples were ground to fine powder (particle size of 8.04 Å), pressed to the pellet form (the diameter and the thickness of the pellets are 10 mm and 1 mm respectively), and sintered at 1250 °C for 24 h. To get the better homogeneity in the samples, this sintering procedure was repeated three times. Experimental details and structural analysis has already been reported elsewhere [23]. The morphological studies of these samples were carried out by scanning electron microscope (SEM) (JOEL scanning Microscope, Model JSM-6490LV) operating at voltage of 25 kV. The average grain size of the samples was measured using the IMAJEJ software. A Hitachi U3300 spectrophotometer was used to study the UV–Vis properties. Fluorescence spectrometer (F-7000 Hitachi) was used to study the photoluminescence properties exiting with its xenon lamp at 325 nm. Vibrating sample magnetometer (VSM-PPMS) of Quantum Design with sensitivity up to 10^5 emu/g (field 100 Oe both in field-cooled (FC) and zero-field-cooled (ZFC)) conditions was used to study the temperature-dependent magnetization (10–300 K). Magnetization versus magnetic field curves were traced at fixed temperatures (10 and 300 K).

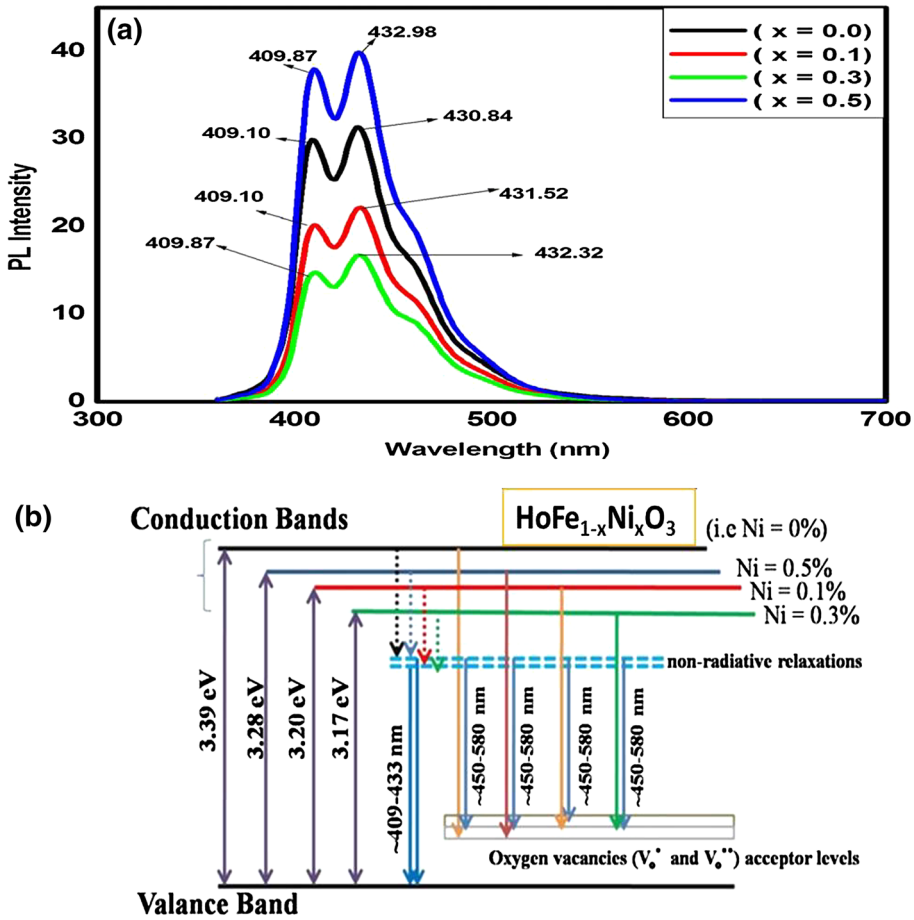

Fig. 3 **a** Room-temperature PL emission spectra of $HoFe_{1-x}Ni_xO_3$ ($x = 0.0, 0.1, 0.3, 0.5$). **b** Band diagram of $HoFe_{1-x}Ni_xO_3$ ($x = 0.0, 0.1, 0.3, 0.5$)

3 Results and discussions

3.1 SEM analysis

Figure 1 shows SEM images of $HoFe_{1-x}Ni_xO_3$ ($x = 0.0$, 0.1, 0.3 and 0.5) compounds and the morphological shows the well-defined grains for $HoFe_{1-x}Ni_xO_3$ ($x = 0.0$, 0.1, 0.3 and 0.5) compounds; however, moderately agglomerated particles are present in the Ni-doped $HoFeO_3$ samples. The average grains size was found to increase with Ni content and dielectric constant as reported earlier [23]. The average grain size measured for $HoFe_{1-x}Ni_xO_3$ ($x = 0.0$, 0.1, 0.3 and 0.5) compounds were 149.30, 159.59, 199.37, and 241.67 nm, respectively. To further examine the presence and the atomic percentage of Ho, Fe, Ni, and oxygen in the prepared samples, dispersive analysis of X-rays (EDAX) was employed. Figure 1 shows the EDAX spectra of $HoFe_{1-x}Ni_xO_3$ ($x = 0.0$, 0.1, 0.3 and 0.5) in which presence of Ho, Fe, and Ni ions are clearly seen. The percentage composition of given elements for all prepared composition as obtained by EDAX listed in Table 1.

3.2 Optical analysis

The UV–Vis spectra of $HoFe_{1-x}Ni_xO_3$ ($x = 0.0$, 0.1, 0.3 and 0.5) are shown in Fig. 2. The optical energy gap (E_g) of the samples was calculated by using the well-known Tauc equation [24],

$$\alpha h\nu = A\left(h\nu - E_g\right)^n$$

where α is the absorption coefficient, ν is the incident beam frequency, A is a constant and n is an index. The value of 'n' confirms the type of transition, which can be assumed to have values, $n = 1/2$, 3/2, 2, and 3. The significance of individual values for n are given as, $n = 1/2$ for a direct allowed transition, $n = 3/2$ for a forbidden direct transition, $n = 2$ for an indirect allowed transition, and $n = 3$ for a forbidden indirect transition [25]. The value of E_g was measured by plotting $(\alpha h\nu)^n$ as a function of $h\nu$, taking n as 1/2, 2, 3, and 3/2, respectively. The only linear fit between $(\alpha h\nu)^n$ as a function of $h\nu$ was obtained for $n = 1/2$. So, we conclude that the present sample has only direct allowed transitions. Band gap energy is presented in Table 2. Figure 2 shows the graph $(\alpha h\nu)^n$ versus

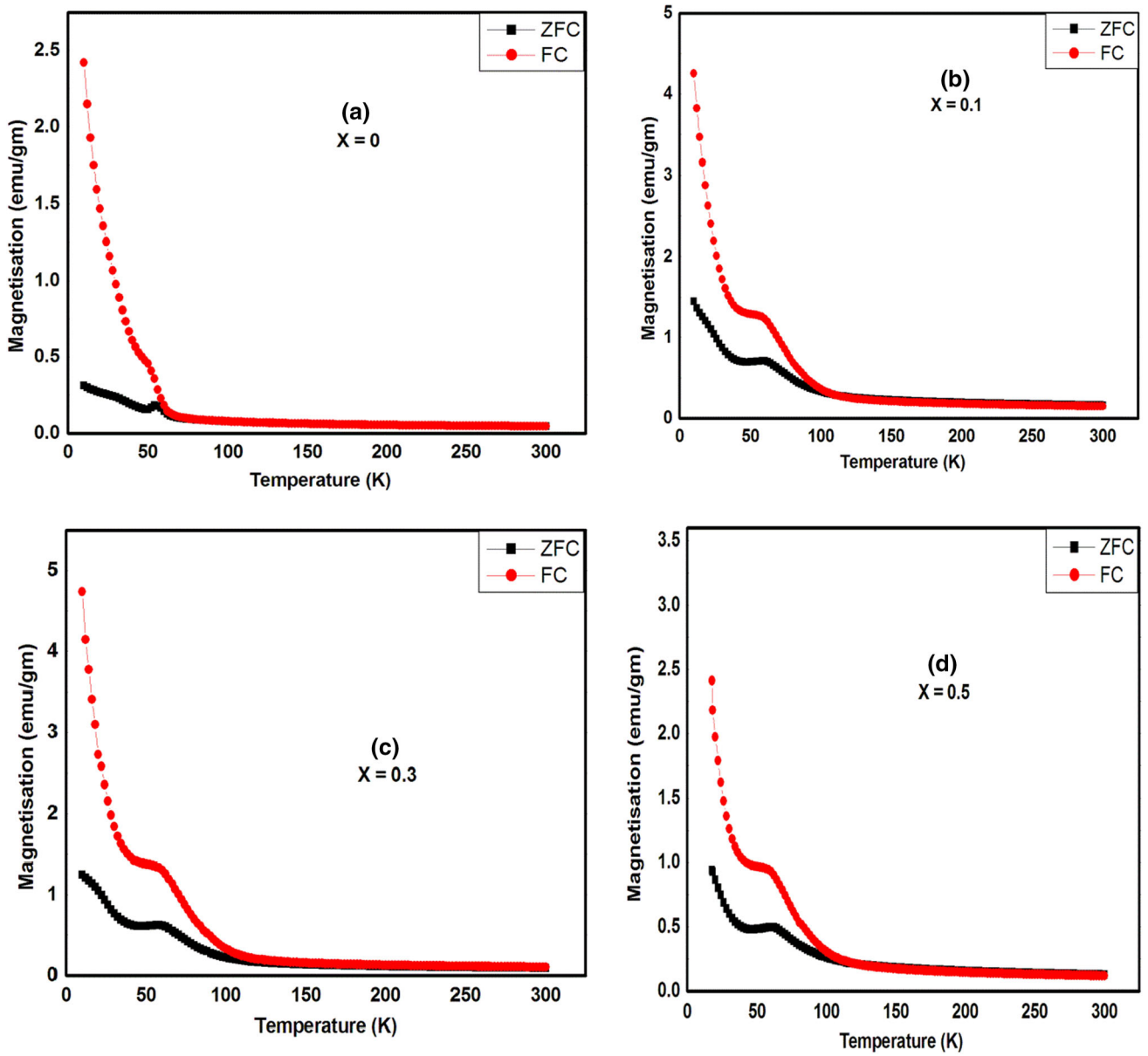

Fig. 4 **a–d** Temperature dependence of zero-field-cooled and field-cooled magnetization plots (in the presence of 100 Oe magnetic field) of $HoFe_{1-x}Ni_xO_3$ ($x = 0.0, 0.1, 0.3, 0.5$)

hv for pristine and doped samples of HoFeO3 made by taking the value of $n = ½$. The linear fit for all the samples has been done, which clearly shows that with increasing Ni-doping absorption edge was found to red-shift. The orthorhombic distortion could be one of the reasons for this observation [25]. In addition, Ni occupies the iron site of FeO_6 octahedra, thus leading to the change of bond angle and bond length (as ionic radii of Fe^{3+} and Ni^{3+} are 0.056 and 0.132 nm, respectively), and Fe–O binding energy will decrease which is favorable for the formation of more oxygen vacancy traps on the surface. The band gap values fall in the range of a number of absorption features observed in the optic spectra of single-crystal orthoferrites. These can be attributed to the charge transfer enhanced crystal field transitions associated with the octahedrally coordinated Fe^{3+} ions [26].

In other words, there is increase in conductivity with Ni doping. Due of doping of Ni ion, band gap decreases due to increase in the density of states which indicates that the correlation length in the conducting network is increasing. This observation indicates that due to the presence of two different homovalent transition metal elements Fe and Ni, the electronic property in the system is driven by the induced disorder effect.

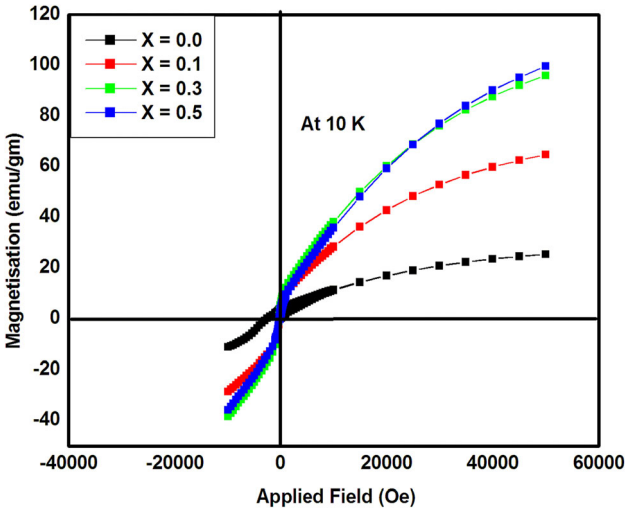

Fig. 5 Magnetization verses applied field plots of $HoFe_{1-x}Ni_xO_3$ ($x = 0.0, 0.1, 0.3, 0.5$) at 10 K

Table 3 Observed magnetization (Ms), retentivity (Mr), coercivity (Hc) and squareness ratio of $HoFe_{1-x}Ni_xO_3$ ($x = 0.0, 0.1, 0.3, 0.5$)

Composition (x)	Ms (emu/g)	Hc (Oe)	Mr (emu/g)	Mr/Ms
0.0	25.50	2659	4.08	0.16
0.1	64.78	197.43	4.31	0.06
0.3	95.19	251.28	5.46	0.05
0.5	99.73	243.61	4.06	0.04

3.3 Photoluminescence study

In order to investigate the various electronic transitions occurring between valence and conduction band, room-temperature photoluminescence (PL) spectra of $HoFe_{1-x}Ni_xO_3$ ($x = 0.0, 0.1, 0.3, 0.5$) were recorded using Xe lamp with wavelength 325 nm as shown in Fig. 3a. The $HoFe_{1-x}Ni_xO_3$ emit stable and high-intensity blue light (visible light emission) with PL peaks at 409.10 and 430.84 nm for $x = 0.0$, 409.10 and 431.52 nm for $x = 0.1$, 409.87 and 432.32 nm for $x = 0.3$ and 409.87 and 432.98 nm for $x = 0.5$ as shown in Fig. 3a. These peaks correspond to band edge emission in the synthesized samples. Photoluminescence studies demonstrate O vacancy related emission with wavelength ranging from 392 nm to 570 nm [27–30]. From band diagram (Fig. 3b), it is observed that the emission intensity of the observed peaks reduces with doping of Ni in $HoFeO_3$. The area under the PL spectra is directly proportional to defects. From Fig. 3a it is observed that the peak intensity decreases up to the composition $x = 0.3$, which means the area under the curve increases which indicates the defects has been increased. However, for $x = 0.5$ the peak intensity increases and hence area under the curve decreased resulting into reduction in number of defects. The photoexcited electrons are preferentially transferred to defects or trap states resulting in non-radiative emission, therefore showing that the emission intensity decreases with Ni-doping concentration [31]. These results could be explained in comparison with XRD results already reported [23]. In emission peaks redshift has been observed in absorption peaks. It is evident from Figs. 2 and 3a that the emission occurs at higher wavelength as compared to absorption. This happens because of non-radiative emission.

3.4 Magnetization measurements

Figure 4 shows the magnetic behavior of Ni-doped $HoFeO_3$ compounds as a function of temperature zero-field-cooled (ZFC) and field-cooled (FC) measurements in the range 10–300 K in an external magnetic field of 100 Oe. In the ZFC mode, the sample was cooled in zero field from 300 to 10 K and after stabilization of the temperature, a field of 100 Oe was applied and then data were recorded while warming the sample. In the FC mode, the sample was cooled down from 300 to 10 K in the presence of a field of 100 Oe and then measurements were carried out while warming in the same field. The Ni-doped and undoped $HoFeO_3$ samples magnetization vs temperature curve (M–T) graph in Fig. (4a–d) shows a characteristic antiferromagnetic transition peak at 50 K after which the sample starts being paramagnetic [32]. Magnetization vs temperature curve for all the samples in ZFC and FC mode shows that Ni-doped samples from $x = 0.0 - 0.5$ samples in the ZFC and FC cycle, the saturation curves begin to separate at the temperature of irreversibility T_{SEP} (shown in Fig. 4a–d), with Ni substitution, Tsep occurs at varied temperature (Tsep = 66, 102, 108 and 120 K for $x = 0.0$, 0.1, 0.3 and 0.5 respectively), from which it concludes that Tsep increases with Ni concentration. The separation effect is related to the impact of the paramagnetic Ho^{3+} ions, whose magnitude becomes more prominent at higher temperatures. The large difference between FC and ZFC at low temperatures suggests an inhomogeneous mixture of a ferromagnetic and antiferromagnetic rather than a distinct ferromagnetic or antiferromagnetic long range order. The M–T curves shows that the magnetization of $HoFe_{1-x}Ni_xO_3$($x = 0.0, 0.1, 0.3, 0.5$) can be described as the sum of two terms one term mainly due to ferromagnetism of distorted FeO_6/NiO_6 octahedra [33] and the other term is attributed to the paramagnetism of Ho sublattices. The canted antiferromagnetism of the |Fe + Ni| network and the behavior of the Ho sublattice contributes independently to the total magnetization. During the FC cycle, the ferromagnetically interacting transition metal (Fe/Ni)

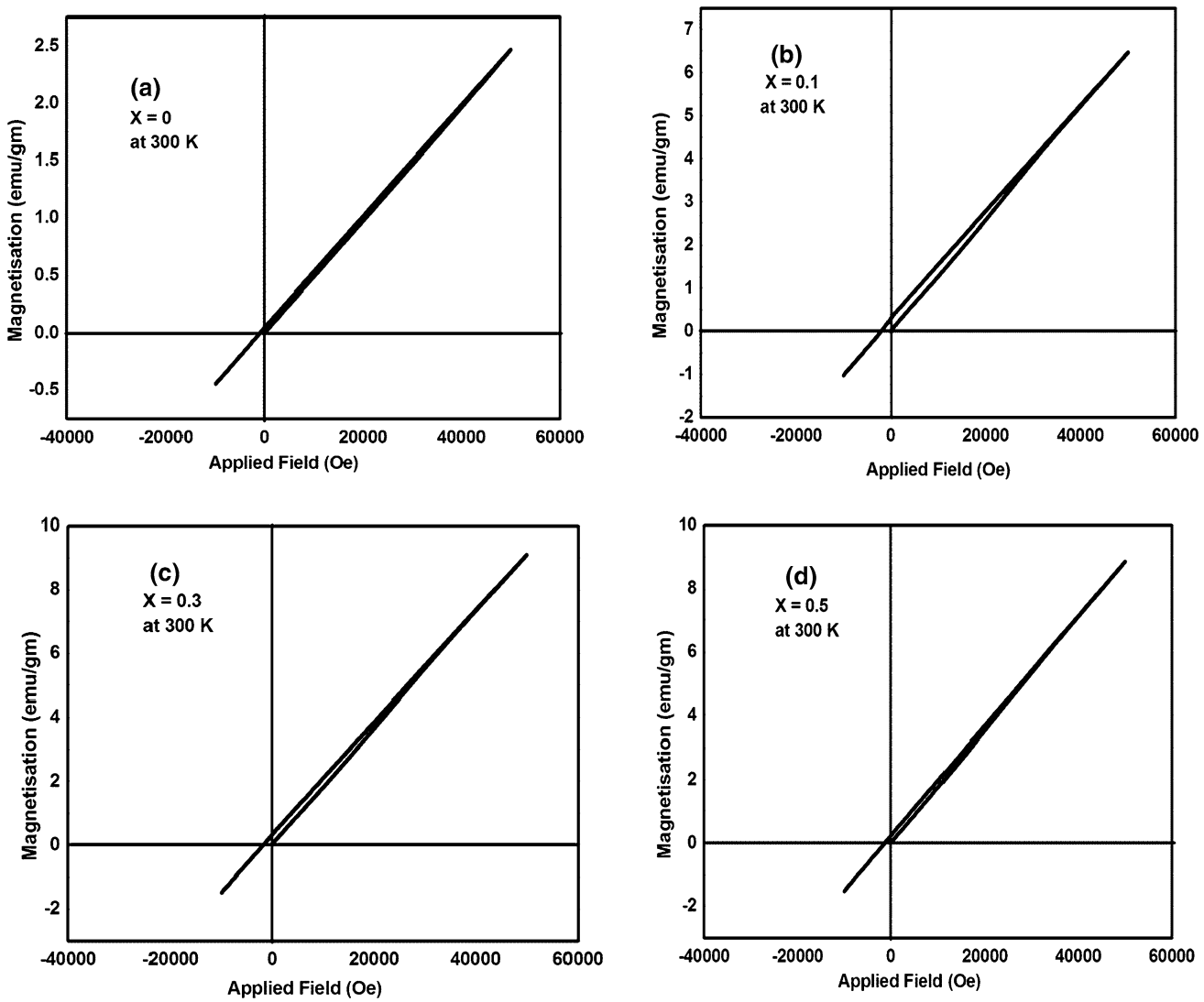

Fig. 6 **a–d** Magnetization verses applied field plots of $HoFe_{1-x}Ni_xO_3$ ($x = 0.0, 0.1, 0.3, 0.5$) at 300 K

sublattices will impose a local field over Ho moments. Hence the resultant magnetization is the superposition of magnetic moments at both the sublattices (transition metal/rare earth). Doping of Ni at Fe site results into the magnetic contribution due to the frustration from two different sublattice phases of transition metal sublattices, in which doping of Ni modulates the ferromagnetism due to Fe–Mn interaction, and paramagnetism from Ho sublattice, which has also been similarly reported by Tokura et al. [34] where it depicts magnetic frustration due to exchange competition between ferromagnetic and antiferromagnetic phases.

The M–H plots at $T = 10$ K for $HoFe_{1-x}Ni_xO_3$ ($x = 0.0, 0.1, 0.3, 0.5$) samples are shown in Fig. 5. The magnetic properties of Ni-doped $HoFeO_3$ have been measured from hysteresis loop to get an insight into the alignment of the magnetic domains which contribute to the effective magnetic characteristics of the samples. Various parameters like saturation magnetization, coercivity, and remanent magnetization were obtained from the hysteresis loop and are summarized in Table 3. From the M–H plots it can be observed that saturation magnetization and remanent magnetization increases with the Ni. The coercive field (H_C) was found to decrease with Ni substitution owing to a larger grain size, which results in the reduction in uncompensated spins. The appearance of ferromagnetism in these samples at low temperature (10 K) may be attributed to the canting of the antiferromagnetically ordered spins by the structural distortion [35]. The change in magnetization of the prepared samples may be described on the basis of change in the hyperfine fields and superexchange interactions. The reason for increasing in saturation magnetization and remanent magnetization may be because of magnetic dilution with a conversion of Fe^{2+} (low spin) valence state to Fe^{3+} (high spin) state on a site

by substitution of the Fe site with Ni ions. In general, the saturation magnetization (Ms) shows a monotonic increase with grain size. Ni-substituted samples are having large grain size resulting in increased Ms.

The value of squareness ratio (Mr/Ms) is estimated from the magnetic data and is shown in Table 3. If the value of squareness ratio is equal to 0.5 or above, it indicate that all the prepared material are in the single domain, while the value is below 0.5 which may be attributed to the formation of multidomain structure. It is observed that the value of squareness ratio in these materials is below 0.5 indicating the multidomain structure.

A remarkable change occurs at 300 K (Fig. 6a–d), where the magnetization shows linear behavior with magnetic field, indicating that the overall magnetic behavior is paramagnetic type. The dramatic change in the magnetization curves shows that, at higher temperature, the paramagnetic behavior of Ho sublattices dominates over the system. Finally, M–H measurements performed at various temperatures between 10 and 300 K complement the magnetization versus temperature data. The magnetization behavior indicates that these materials represent the spin reorientation phenomena.

4 Conclusion

Solid-state reaction technique was used to synthesize the bulk samples of Ni-doped $HoFeO_3$. The substitution of Ni at Fe site results in significant changes in the physical properties of compound. Results from SEM images reveal that the particles are spherical in shape with distinguishable boundaries and the average grain size increases with Ni doping. The shifting of absorption edge toward higher wavelength (redshift) has been observed with Ni concentration. At lower temperatures, the samples are ferromagnetic and at higher temperature these samples show paramagnetism. The large difference between FC and ZFC at low temperatures suggests an inhomogeneous mixture of a ferromagnetic and antiferromagnetic rather than a distinct ferromagnetic or antiferromagnetic long range order. Saturation magnetization (M_S) increases and coercive field (H_C) decrease with the increase in Ni resulting in the reduction of uncompensated spins. The value of squareness ratio in this material is below 0.5 indicating that multidomain structure.

Acknowledgments Authors thank Dr. Alok Banerjee IUC, CSR, Indore, for the magnetic measurements. Authors would also like to thank Director IUAC, New Delhi, for necessary experimental facilities and Director NIT Srinagar for encouragement provided during work.

References

1. R.L. White, J. Appl. Phys. **40**, 1061 (1969)
2. V. Kumar, S. Som, L.P. Purohit, O.M. Ntwaeaborwa, H.C. Swart, J. Alloy. Compd. **594**, 32–38 (2014)
3. K. Sultan, M. Ikram, K. Asokan, Vacuum **99**, 251–258 (2014)
4. J.K. Vassiliou, Solid State Chem. **81**, 208 (1989)
5. J.B. Torrance, Phys. Rev. B. **45**, 8209 (1992)
6. V. Kumar, A.K. Bedyal, J. Sharma, V. Kumar, O.M. Ntwaeaborwa, H.C. Swart, Appl. Phys. A **116**, 1785–1792 (2014)
7. K. Sultan, M. Ikram, S. Gautam, H.K. Lee, K.H. Chae, K. Asokan, J. Alloy. Compd. **628**, 151–157 (2015)
8. K. Sultan, Z. Habib, A. Jan, S.A. Mir, M. Ikram, K. Asokan, Adv. Mat. Lett. **5**(1), 9–13 (2014)
9. S. Geller, E.A. Wood, Acta Crystallogr. **9**, 563 (1956)
10. L. Neel, Acad. Sci. Paris **239**, 8 (1984)
11. N.Y. Vasanthacharya, P. Ganguly, C.N.R. Rao, J. Solid State Chem. **53**, 140 (1984)
12. Y.S. Didosyan, H. Hauser, G.A. Reider, R. Glatz, H.J. Wolfmayr, Appl. Phys. **93**, 8755 (2003)
13. R. Kumar, R.J. Choudhary, M.W. Khan, J.P. Srivastava, C.W. Bao, H.M. Tsai, J.W. Chiou, K. Asokan, W.F. Pong, J. Appl. Phys. **97**, 093526 (2005)
14. R. Kumar, R.J. Choudhary, M. Ikram, D.K. Shukla, S. Mollah, P. Thakur, K.H. Chae, B. Angadi, W.K. Choi, J. Appl. Phys. **102**, 073707 (2007)
15. A. Bashir, M. Ikram, R. Kumar, P. Thakur, K.H. Chae, W.K. Choi, V.R. Reddy, J. Phys.: Condens. Matter **21**, 325501 (2009)
16. S.A. Mir, M. Ikram, K. Asokan, RSC Adv. **5**, 85052–85094 (2015)
17. Z. Habib, M. Ikram, K. Majid, K. Asokan, Appl. Phys. A **116**, 1327–1335 (2014)
18. R.M. Bozorth, V. Kramer, Coloque International de Magnetisme, Grenoble, suppl. J. Phys. Radium **20**, 329 (1959)
19. W.C. Koehler, E.O. Wollan, M.K. Wilkinson, Phys. Rev. B **118**, 58–70 (1960)
20. J. Mareschal, J. Sivardiere, J. Phys. (paris) **30**, 967–973 (1969)
21. S.C. Parida, S.K. Rakshit, Z. Singh, J. Solid State Chem. **181**, 101–121 (2008)
22. M. Eibschutz, S. Shtrikman, D. Treves, Phys. Rev. **156**, 562 (1967)
23. Z. Habib, K. Majid, M. Ikram, K. Asokan, J. Electron. Mater. **44**(4), 1044–1053 (2015)
24. S. Ahmed, M. Nasir, K. Asokan, M. S. Khan, M. Zulfequar, RSC Adv. 1–10 (2015)
25. J.S. Zhou, J.B. Goodenough, Phys. Rev. Lett. **96**, 247202 (2006)
26. F.J. Kahn, P.S. Pershan, J.P. Remeika, Phys. Rev. Lett. **21**, 804 (1968)
27. L. Dai, X.L. Chen, J.K. Jian, M. He, T. Zhou, B.Q. Hu, Appl. Phys. A Mater. Sci. Process. **75**, 687 (2002)
28. J.S. Jeong, J.Y. Lee, C.J. Lee, S.J. An, G.C. Yi, Chem. Phys. Lett. **384**, 246–250 (2004)
29. X.C. Wu, J.M. Hong, Z.J. Han, Y.R. Tao, Chem. Phys. Lett. **373**, 28 (2003)
30. M.J. Zheng, L.D. Zhang, G.H. Li, X.Y. Zhang, X.F. Wang, Appl. Phys. Lett. **79**, 839 (2001)
31. J. Singh, N.K. Verma, J. Supercond. Nov. Magn. **25**, 2425–2430 (2012)
32. L. Jiang, Ceram. Int. **38**, 3667–3672 (2012)
33. A. Wu, H. Shen, J. Xu, L. Jiang, L. Luo, S. Yuan, S. Cao, H. Zhang, J. Sol-Gel. Sci. Technol. **59**, 158–163 (2011)
34. Y. Tokura, Phys. Today **56**, 50 (2003)
35. K. Ueda, H. Tabata, T. Kawai, Appl. Phys. Lett. **75**, 555 (1999)